



Experimental and numerical study on the performance and flow pattern of different Savonius hydrokinetic turbines with varying duct angle

Aditya Kumar Nag¹ · Shibayan Sarkar¹

Received: 9 July 2019 / Accepted: 23 November 2019 / Published online: 4 December 2019
© Springer Nature Switzerland AG 2019

Abstract

In this study, three different types of Savonius rotors viz. Savonius hydrokinetic turbine (SHKT), modified Savonius hydrokinetic turbine (MSHKT) and helical Savonius hydrokinetic turbine (HSHKT) are compared based on the performance. The analysis is done experimentally as well as numerically, where experimental domain ceases. Performance of rotors is also evaluated with and without applying duct as an augmentation technique in the flow channel. Experimentally, MSHKT and HSHKT produce 2.74% and 9.04% more energy than SHKT for 1 ± 0.2 m/s. Uncertainties in TSR, C_p and C_t of rotor are 3.05%, 4.39% and 5.35% for the experiment. It is found that HSHKT has better performance than others. Whereas, with duct, performance of HSHKT improves 48.08% more energy than SHKT. The insight of the hydrodynamic behavior considering wake formation, flow separation and vortex formation of the stream flow surrounding to the rotor is also explained using velocity contour, velocity vector and pressure plot. Inlet velocity of 1 ± 0.2 m/s increases by 27.5%, 28%, 29%, 32% and 34%, respectively, for duct angle 20° , 23° , 26° , 29° and 32° . Simultaneously, low-pressure zone increases which leads to extend the formation of the vortex far from rotor and helps to generate higher C_p for HSHKT as 28.63%, 16.16%, 43.01%, 50.13% and 82.32%, respectively.

Keywords Savonius hydrokinetic turbine · Vortex · ANSYS-CFX · Duct · Performance parameter · Flow characteristics

List of symbols

a	Overlap distance (m)
A	Projected area of the rotor (m^2)
$a_1, a_2, a_3 \dots a_n$	Power coefficients of variables
$A_{c/s}$	Cross-sectional area of the flow
AR	Aspect ratio
D	Rotor diameter (m)
$D_{C/H}$	Characteristic diameter (m)
D_o	End plate diameter (m)
d_r	Diameter of the rope (m)
D_s	Shaft diameter (m)
Fe	Froude number
g	Acceleration due to gravity ($=9.81 \text{ m/s}^2$)
H	Rotor height (m)

H_w	Height of the flowing water (m)
N	Number of rotation of rotor per minute (RPM)
p/q	Blade shape factor
P_{rotor}	Shaft power (W)
P_{wetted}	Wetted perimeter of the rotor (m)
R	Radius of the rotor (m)
$R_{C/H}$	Characteristics radius (m)
Re	Reynolds number
r_p	Radius of the pulley (m)
t	Blade thickness (t)
T	Torque (Nm)
t_{end}	End plate thickness (m)
T_{width}	Top width of the channel (m)
u_j	Components of velocity in the corresponding direction (m/s)
u_x, u_y, u_w	Fluctuation of the velocity in the x , y and z -direction respectively (m/s)
V	Free stream velocity (m/s)
V_1	Upstream velocity of the flume (m/s)
V_2	Downstream velocity of the flume (m/s)
W	Width of the channel (m)

✉ Shibayan Sarkar
shibayan.sarkar@gmail.com

Aditya Kumar Nag
adityakumarnag2013@gmail.com

¹ Department of Mechanical Engineering, Indian Institute of Technology (ISM), Dhanbad 826004, Jharkhand, India

W_{SS}	Tension in slack side (kg)
W_{TS}	Tension in tight side (kg)
$X_1, X_2, X_3 \dots X_n$	Independent sensitive coefficients
θ	Rotor twist angle
ρ	Density of the fluid (= 1000 kg/m ³)
ω	Angular velocity of the rotor (rad/s)
$\omega_1, \omega_2, \omega_3 \dots \omega_n$	Uncertainties in the independent variables

1 Introduction

Studies reveal that, in 2018, across one billion people failed to access electricity which is the requisite of modern sustenance (IEA 2018; Global energy statistical yearbook 2018; The World Bank Data 2018). Renewable energy can play a vital role in solving the problem. It is reliable, socio-economic, and it has a diminutive impact on the environment. Studies show that in present days, renewable energy has the fastest growth in electricity production, out of which hydropower is going to contribute 16% of the electric generation globally by 2023 (REN21 2018; Nag and Sarkar 2018). Hydrokinetic turbines (HKT) are the future of the micro-hydropower plant and the subsidiary elements of renewable energy. Hydrokinetic energy utilizes the kinetic energy of the flowing water in the canals, river, tidal current and ocean waves. According to the Bentz theory, maximum power extracted by the rotors from the free stream is 59.3% of the available kinetic energy of the free stream. These types of turbines are also known as low-pressure and ultra-low head turbines (Rauh and Seelert 1984; Garrett and Cummins 2008). However, the maximum power limit exceeds when the free stream velocity is utilized an utmost, and proper selection of HKTs is done with suitable modifications (Venell 2013; Cuerva and Sanz-Andrés 2005). In general, classification of HKTs is based on the type of flow. Turbine axis which is parallel to the stream flow is called axial flow turbine and if aligned orthogonally to the stream flow is called cross-flow turbine. Axial flow turbines have variation based on a number of blades viz. two-bladed turbines, three-bladed turbine, and multi-bladed turbine. However, cross-flow turbines are also classified further based on their design viz. Savonius turbine, Darrieus turbine, Gorlov turbine and H-Darrieus-type turbine (Khan et al. 2009; Vermaak et al. 2014; Guney and Kaygusuz 2010; Yuce and Muratoglu 2015). The Savonius turbine is one of the basic types of cross-flow turbine, commonly used because of its simple design, relatively low operating speed, good starting ability, easiness of fabrication and installation (Golecha et al. 2011; Wahyudi et al. 2015). In addition, hydrokinetic turbines are classified based on axis alignment, viz. vertical axis turbine and horizontal axis turbine. This vertical axis Savonius hydrokinetic turbine (SHKT) is the conventional one

and has low efficiency. To improve the performance of this vertical axis hydrokinetic turbine, certain design modifications are adopted (Table 1), such as variation in aspect ratio, overlap ratio, twisted blade angle (Kumar and Sarkar 2016a, b). Design modification of the Savonius turbine produces the following types of turbine viz. helical Savonius hydrokinetic turbine (HSHKT) and modified Savonius hydrokinetic turbine (MSHKT). After modification of parameters, SHKTs are generally compared with the conventional Savonius rotor. Moreover, following augmentation techniques are also adopted for better performance of turbine viz. variation in the channel width, application of duct, nozzle and deflector plates in both upstream and downstream, several numbers of deflector plates with systematic positions as well as angular arrangement, multi-stage turbines and arranging the turbines in array (Kumar and Saini 2017; Gaden and Bibeau 2010; Kumar and Sarkar 2016a, b, 2017). Maldonado et al. (2014) showed that implementing augmentation deflector in upstream of the Savonius rotor may increase 20% flow velocity.

Several comparative studies were conducted on different hydrokinetic turbines based on their performances. Talukdar et al. (2018) proved experimentally that HSHKT attains higher starting ability and higher coefficient of power (C_p) compared to SHKT because of its blade design modification on chord length, aspect ratio and angle of twist. do Rio et al. (2013) suggested a better rotor model by optimizing blade length and twist angle for better performance. Kamoji et al. (2009) have done design modification by removing the central axis shaft from MSHKT and found that it has higher C_p than normal MSHKT. Harries et al. (2016) experimented on novel drag driven vertical axis tidal turbine and SHKT. It is found that C_p and C_t of SHKT increase with increasing blockage ratio. Shimokawa et al. (2012) experimentally showed that nozzle increases the C_p , the coefficient of torque (C_t) and reduces flow separation from the blade profile, which produces less negative lift (at the returning blade) and reduces the downstream height of water. As a result, performance of the SHKT increases. Sarma et al. (2014) showed a detailed study of the velocity distribution of stream flow surrounding the blades which provide the insight of the design of the SHKT. Some study clarified on disturbances and vortex interactions of the stream flow surrounding the rotor blade (Alom and Saha 2018; Wahyudi et al. 2015), without mentioning about the performance parameters of the turbine or did not compare with other turbine rotors.

Besides the expensive experimental approach, numerical analysis became popular as an alternate method to explore the performance of HKTs. To replicate the behavior of HKT, researchers preferred the computational fluid dynamics (CFD) simulations in ANSYS CFD-CFX software (Hosseini and Goudarzi 2018; D'Alessandro et al. 2010). It produces more insight into flow separation, wake

Table 1 Modifications of Savonius hydrokinetic turbine design parameters and channel parameters for performance enhancement

Type of parameters	Performance increase criteria	Major findings	Research gap	References
Design Parameter of rotor: Number of blade, shape of blade (elliptical),	In two-blade rotor, elliptical shaped blade is used. Further, conventional shaped three blades are used instead of two through an experimental analysis	(i) Improvement of C_p by 28.6% and 39.2% in case of two-bladed (elliptical) and three-bladed rotors. (ii) Vortex occurring due to third blade affects the rotor performance	More than three numbers of blades are not tested. Other shaped blades are not tested	Talukdar et al. (2018)
Optimal blade shape	Modified shapes of the rotor are used for enhanced performance and good starting ability both, using optimization study	(i) Optimal rotor shape is proposed (ii) C_p value increases with TSR better than conventional Savonius rotor (iii) While flow velocity increases, at TSR 1.4 C_p increases up to 75.4%. This indicates Maximum $C_p (C_{p_{max}})$ may be achieved at $TSR > 1$ (iv) Self-starting ability is increased at any rotational angle position of the rotor	Experimental validation is not done for the proposed shaped blade. The blade is difficult to manufacture for commercial us	Mohamed et al. (2011)
Angle of twist (θ)	Different twisted blade angles (θ) are considered in a numerical analysis	(i) $C_{p_{max}}$ varies with twist angle. Highest $C_{p_{max}}$ obtained at $\theta = 12.5^\circ$ (ii) Pressure and velocity contour plot show that pressure difference across the rotor generates drag force responsible for rotation of rotor	Mechanisms of wake and vortices generation are not discussed	Kumar and Saini (2017)
Overlap ratio (α)	Influence of the overlap ratio in the performance of the rotor by numerical study.	(i) C_p attains its highest value at an optimum overlap ratio ($\alpha = 0.15$) (ii) The excessive overlap ratio leads to decrease in the C_p due to the less wetted area of the rotor	2D simulations are carried out which do not take into account aspect ratio and turbulence intensity	Akwa et al. (2012)
Multi staging of rotor	Numerical and experimental analysis of multi-stage Savonius rotor to choose the most effective rotor	(i) C_p and C_t increase with the increase in the number of stages, keeping the diameter same (ii) Maximum velocity and pressure acted on the rotors are recorded (iii) Minimum turbulence is obtained at one stage and two stages	Aspect ratio not maintained, while the study is conducted. Optimized number of staging is not suggested	Frikha et al. (2016), Menet (2004)
Flapping blade/slatted blade	Numerical analysis is done to increase the effective incident flow area and to reduce the resisting flow area	(i) At low operating conditions, C_p increases (ii) On driving blade higher pressure is observed which is responsible for the acceleration of the turbine	When $TSR > 1$ the resistance moment on the rotor is larger than the driving moment provided by the free stream	Li and Zhou (2017)

Table 1 (continued)

Type of parameters	Performance increase criteria	Major findings	Research gap	References
Channel modification: deflector plates	Experimental study on the Optimized positioning of deflector plates	(i) Optimal position of the deflector blade (in advancing blade side) is reported as $1.8R$ (R , radius of rotor) and at 50° inclination along the direction of flow (ii) Deflector plate increases $C_{p_{max}}$	Optimum position of the deflector plate in returning blade side is not discussed	Kailash et al. (2012); Golecha et al. (2012)
Thick deflector plate	Improve the performance of the Savonius rotor and to minimize the upstream drag force at the returning blade	(i) Improvement in the C_p is obtained due to the less pressure obtained at the returning blade (ii) Due to the curved shape of the deflector free stream flow diverted towards the advancing blade	Experimental validation is missing. Complex geometry is suggested	Kerikous and Thevenin (2019)
Guide vanes	Experimental and numerical studies are conducted to find the way of restricting negative torque generation using guide vane	(i) The value of the $C_{p_{max}}$ and torque generated are enhanced due to the guide vane (ii) Much more stable rotation is achieved	2D numerical simulations are conducted without discussing the influence of flow phenomenon like wake and vorticity due to introduction of guide vane	Altan and Atilgan (2008)
Duct	Bidirectional and ducted nozzle are used in channel for the performance improvement carried out numerically	(i) Ducted channel increases upstream velocity and increases pressure difference (ii) $C_{p_{max}}$ value ducted nozzle turbine is increased (iii) The drag force acted on the returning blade at the upstream of rotor is reduced	Experimental implementation of the duct is missing	Elbatran et al. (2017), Alidadi and Calisal (2014)
Varying duct angle	Variation in the duct angle and positioning of the rotor to increase the performance numerically	(i) Power increases when the convergence angle of the duct increases (ii) Maximum C_p is found at the throat of the duct	Experimental validation is needed and influence of the duct over rotor is not attempted	Malipeddi and Chatterjee 2012
Hump	Experimental analysis is done for the Performance improvement of the Savonius turbine by changing the cross-sectional area of the duct	(i) Increase in the power output of the turbine by 236% on increasing 55% of the hump height (ii) $C_{p_{max}}$ values increases by 27% on decreasing 52% of the channel area	General discussions are done only at the upstream of the rotor, also detailed analysis need to be done at the downstream stream side of the rotor	Patel et al. (2019)
Varying duct profile	Different cross-sectional profiles are tested for duct augmentation, to increase the self-starting ability	(i) Increment in the free stream velocity at the upstream of the rotor (ii) Even at low free stream velocity self-starting ability is good	Variations in each cross-sectional profile are not performed	Ponta and Dutt (2000)

characteristics, vortices and very less discrepancy in the performance of the turbine (Bianchini et al. 2017; Behrouzia et al. 2015). Kumar and Saini (Kumar and Saini 2017) suggested the $k-\epsilon$ turbulence model for the CFD analysis for the HKT. Elbatran et al. (2017) designed different types of the duct and evaluated their performance on SHKT computationally. They used SST $k-\omega$ turbulence model to explore boundary layer separation and reported that 78% of the gain in power is observed when the duct is implemented. Driss et al. (2014) compared the performance of ducted nozzle mounted SHKT with the conventional SHKT using the $k-\epsilon$ turbulence model and validated the same results with experiments. This numerical study reported vortices distribution longitudinally to the fluid flow surrounding the SHKT. However, maximum vorticity is obtained across the SHKT, just downstream of the advancing blade. Moreover, the wake zone is found in the downstream of the SHKT. Birjandi et al. (2013) found that flow stream angle of attack at the upstream of SHKT increases flow separation; as a result, the lift force reduces (at the advancing blade). Simultaneously vortex also increases, which leads to the reduction in the C_p and C_t , and hence performance decreases. Gorle et al. (2016) illuminate the effect of the blade–vortex interaction across the turbine which restricts the rotor rotation.

Following research gaps are not found during literature review (Table 1): (1) effect of adjustable blade on the performance of Savonius hydrokinetic turbine, (2) influence of more than three numbers of blades on the performance of the rotor, (3) role of wake and vortices on the performance of Savonius hydrokinetic turbine, (4) performance comparison of different Savonius hydrokinetic rotors, (5) optimized number of staging and its positioning considering same aspect ratio, (6) rotor simulations with changing aspect ratio in view of turbulence intensity influence, etc.

In view of efficient renewable energy generation, a comparative performance study of different Savonius turbine rotors is a pertinent problem. Open literature does not provide any clear idea of flow phenomenon happening around the blades influencing the rotor performance. Therefore, the aim of this study is set to explore the performance of different Savonius hydrokinetic turbine rotors with and without the application of duct, numerically as well as experimentally. Simultaneously hydrodynamic effects are also explained surrounding the rotor during operation. Further, a comparison study may be done to evaluate the performance of the rotors, within the experimental limit and as well as beyond the experimental limit with the help of a simulation study. Moreover, Savonius rotor hydrodynamics, duct angle effect, vortices and wake characteristics on SHKT may be explained. Therefore, novelty of this study is to conduct a comparative study of the performance of three different Savonius rotors with the detailed description of the

flow phenomenon surrounding the blades, numerically with experimentally, with and without the influence of channel modification parameter like duct augmentation.

2 Methodology

In this study, numerical and experimental analyses are done to evaluate the performance of the Savonius hydrokinetic turbine (SHKT), helical Savonius hydrokinetic turbine (HSHKT) and modified Savonius hydrokinetic turbine (MSHKT) with and without implementing augmentation technique like a converging–diverging duct. Both the analyses are performed considering the distance of the rotor (L) from the initiation of duct convergence as 4 times the diameter of the rotor (D). Performance of the rotor is mainly decided based on the power generation capacity of the rotor. Fluid flow pattern surrounding the rotor and energy conversion is mainly governed by the hydrodynamic theory of rotor.

2.1 Hydrodynamic theory of rotor

Flow pattern surrounding the rotor in operation is shown in Fig. 1. Top view of the rotor shows that the flow passing through the rotor transmits kinetic energy to the advancing blade. Whereas, the front view shows the total specific energy in the stream flow strikes at the advancing blade and leaves with the reduction in the depth of the stream flow.

At the upstream of the rotor, the advancing blade experiences flow velocity; while at the concave surface, stagnation pressure develops. At the tip of the advancing blade, flow separation takes place due to the low pressure. As a consequence, a pressure difference occurs in between the upstream and downstream of the rotor, which helps to rotate the turbine. Due to the pressure difference, vortices form at the upstream of the advancing blade. This spinning motion of the fluid particles is carried by the wake in downstream. Simultaneously, at the downstream of the rotor, flow separation occurs at the tip of the advancing blade, towards the direction of flow. This creates negative pressure near the downstream of the returning blade. Meanwhile, advancing flow strikes the returning blade also which is convex in geometry, along the flow direction, with positive pressure. As long as the pressure difference exists, the turbine rotates. Simultaneously, the Coanda effect is also observed, which has the tendency to make the fluid particle stay attached to a convex surface. This fluid particle experiences high pressure due to the adjacent fluid layer and low pressure on the inner part of the fluid particle attached to the convex surface. Due to the pressure difference, fluid particle experiences a centripetal force which causes an increase in the torque. Moreover, due to the high-pressure zone on the concave side

of the upstream and low-pressure zone on the convex side of the downstream, the advancing blade experiences drag force and returning blade experiences negative drag force. The overall resultant of the drag force provides the rotation to the rotor.

In general, wake formation carries vortices which lead to the vortex shedding. As the flow impinges to the body, it generates first stagnation point (higher pressure) at the upstream of the rotor, second stagnation point (moderate pressure) is just after downstream at the rotor and third stagnation point (low pressure) is at downstream away from the rotor. Due to pressure difference at the second and third stagnation points, the flow has a tendency to proceed along the flow direction. However, simultaneously, vortices influence the flow to turn towards the upstream direction due to circulation. As long as the pressure difference at the second and third points is higher, the above-said effect on the fluid gets reduced and it obstructs the flow to be returned towards the rotor. Therefore, the distance between the second and third stagnation point is preferred to be higher to avoid any obstruction to torque generation by the rotor.

On the other hand, if the volume of the fluid striking the blade is considered, it is clear from Fig. 2a that one part of the fluid is striking in the advancing blade directly, and another part is striking the returning blade. The part striking the returning blade again divides into two halves. One half is gliding over the returning blade and leaves the rotor. Another half is joining the fluid flow striking the advancing blade which results in stagnation pressure. This creates positive pressure, which is responsible for the rotation of fluid. The position of the rotor blade in Fig. 2a is 90° along the flow direction. As the swept area of the rotor is maximum at 90° , it exerts maximum drag force in the advancing blade and produces maximum power. Figure 2b shows the developments of power over one complete rotation of the rotor from 0° to 360° . Power generation follows a sinusoidal curve from 0° to 360° . Moreover, because of the implementation of the duct, the angle of attack of the free stream at the tip of the advancing blade became higher, which helps to increase the intensity of the power.

In order to carry out the performance analysis, both numerical and experimental studies are conducted. The details of the methodology are described in a flowchart in Fig. 3. For numerical analysis, ANSYS CFD-CFX is used to develop flow simulation and to study the behavior of the different HKT rotor under different operating conditions. This study complies 3D modeling of flume and rotor, and mesh generation of the 3D model. Further, initial and boundary conditions are applied in the setup for CFX and the results are obtained for different operating conditions. Whereas, for the experimental investigation, an experimental setup is designed and fabricated.

The experimental setup consists of the flume, different HKT rotors, measuring sensors viz. flow meter,

dynamometer, non-contact-type tachometer, etc. In the setup, turbines and all the measuring devices can be moved to x - y - z -direction using mounting trolley while performing the experiments. Values obtained in the experiment are used to validate the results of the numerical study. Whereas, the numerical analysis predicts some results, which are beyond the capacity of the experimental setup. Details of the numerical study are discussed as follows.

2.2 Numerical study

To study the performance of SHKT, whole experimental setup and their analysis are replicated in the computational domain in ANSYS CFD-CFX. In general, to solve turbulence flow problems, a proper model has to be selected based on the Reynolds number, flow geometry and flow separation. In this study, the model is adopted as the flow solver to simulate the unsteady incompressible flow of fluid accounting turbulence and viscosity. The k - ϵ model is preferably used to solve the flows involving rotational body and boundary layer phenomenon (Launder and Spalding 1983). Moreover, k - ϵ model has capability to solve the problems involving the fluid flow through the proximity of the complex geometries, such as turbine blades (Sarma et al. 2014; Driss et al. 2014). Savonius turbine blades have sharp corners and curved edges. This study tries to represent flow pattern surrounding the blades in rotating condition. Thus, k - ϵ model is opted in this study for the computational simulation in ANSYS software.

In this study, for optimum computation time in ANSYS, the shear stress transport is adopted considering 5% of turbulence intensity. Turbulence intensity gives the proximate results of the turbulence models and also used for flow separation with the different pressure gradient. In the computational analysis, the flume is defined as a stationary domain. Whereas, fluid is considered as flowing domain and rotor is enclosed with the cylindrical domain provided with the rotational feature. The input of the rotational domain is the angular velocity of the rotor which varies as per the varying loading conditions. These domains are further meshed fully and provided inflation layer on the rotor blade. This interaction between rotor and fluid is studied in respect of variation in velocity and wake characteristics.

Grid independence test for three different rotors is done at different refinement levels. It is tested by assessing the power output by the rotor for different mesh densities. The details of the selected mesh size corresponding to the adopted refinement level 8 for the different rotors are given in Fig. 4 and Table 2. According to the different rotor shape, the variation in the blockage area is covered on the flume. Hence, fluid domain meshes, respectively, to each rotor. Tetrahedral unstructured mesh has been provided for further simulation.

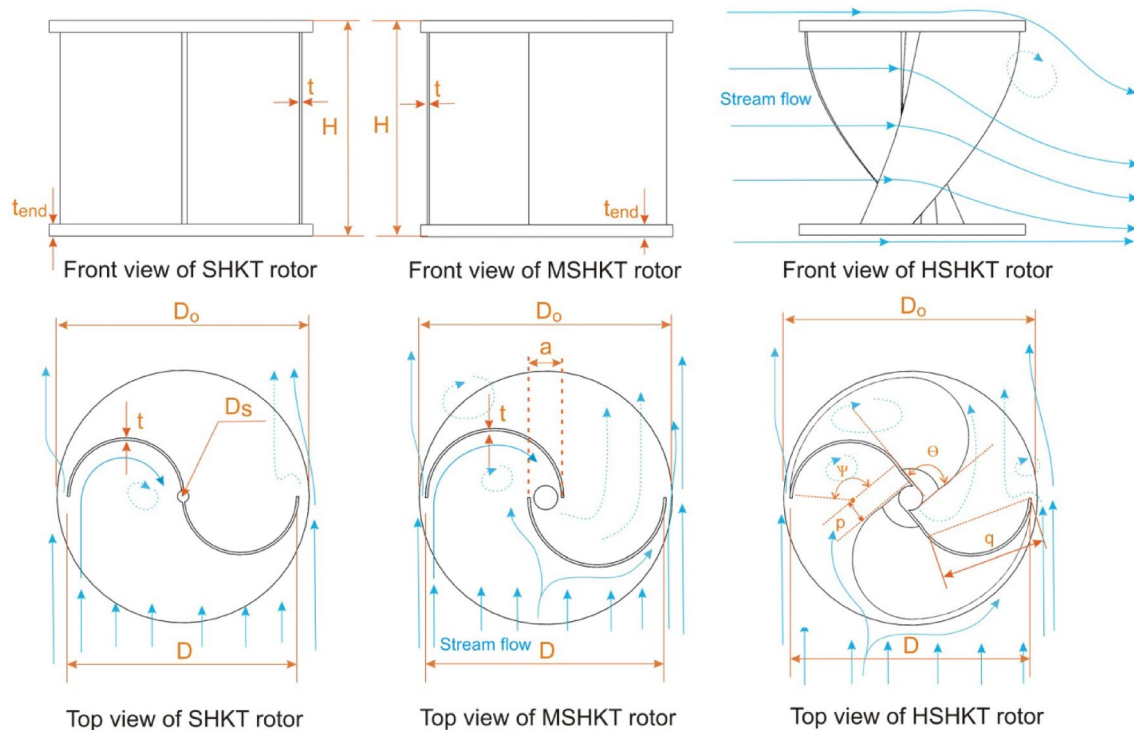


Fig. 1 Notations of SHKT, MSHKT and HSHKT design and stream flow pattern

In the present study simulation, initial and boundary conditions are kept the same for all the cases. At the inlet of the fluid domain, the initial condition is provided as the uniform velocity of 1 m/s, 2 m/s and 3 m/s for atmospheric pressure conditions, i.e., 0 atm. Boundary conditions are provided as a no-slip wall considering smooth roughness. Outlet conditions are provided as 0 atm distributed uniformly which replicates the proximity of the solution. Besides that, some more necessary inputs are implemented, which are shown in Table 3.

From the above numerical study, power and torque are obtained for each time step with the provided number of turbine rotation simulation. Through this analysis, the hydrodynamic flow field surrounding the HKT is examined. It is observed with the help of a velocity contour plot and velocity vector plot which shows the velocity magnitude and direction throughout the flume. This study is extended to show the behavior of different types of HKTs in the presence of stream flow. Moreover, this study could also explore the behavior of HKT rotors after implementation of augmentation techniques, which can further be validated through experiment.

2.3 Experimental study

The experimental setup was fabricated for analyzing the performance of different HKT rotors (Fig. 5a). The

setup is mainly constituted by a flume (rectangular channel), which is further simulated numerically considering the conditions mentioned in Table 3 (Fig. 5b). Reading torque and power at different flow condition is the main objective of this setup, which is done by a dynamometer (Fig. 5c). The cross-sectional dimensions of the open rectangular channel are 6 m × 0.6 m × 0.7 m in which Savonius rotors are placed (Fig. 5d, e). Here, rotors are shown in just immersed condition as water is muddy and recycled water is used for the study; however, experiments are done in full immersed condition. The Savonius rotor is fixed with a frame movable in x -, y - and z -direction (Fig. 5f). Moreover, multiple rotors could be mounted in the flume. The two 10-hp pumps are installed in the setup to supply water to the flume. Two valves are connected separately with each pump to control the discharge. This provides surface fluid flow velocity at the flume test section within a range of 0–2 m/s. The flow is measured by flow meter capable of moving in the x – y – z -direction in the flume. The rotational speed of the rotor is measured by non-contact type tachometer attached with the movable trolley which holds HKT rotor. Rotor torque is measured by the help of dynamometer mounted in the same trolley.

For the present study, hydrokinetic rotors are designed based on the design specification mentioned in Table 4. Description of the nomenclature is shown in Fig. 1 and

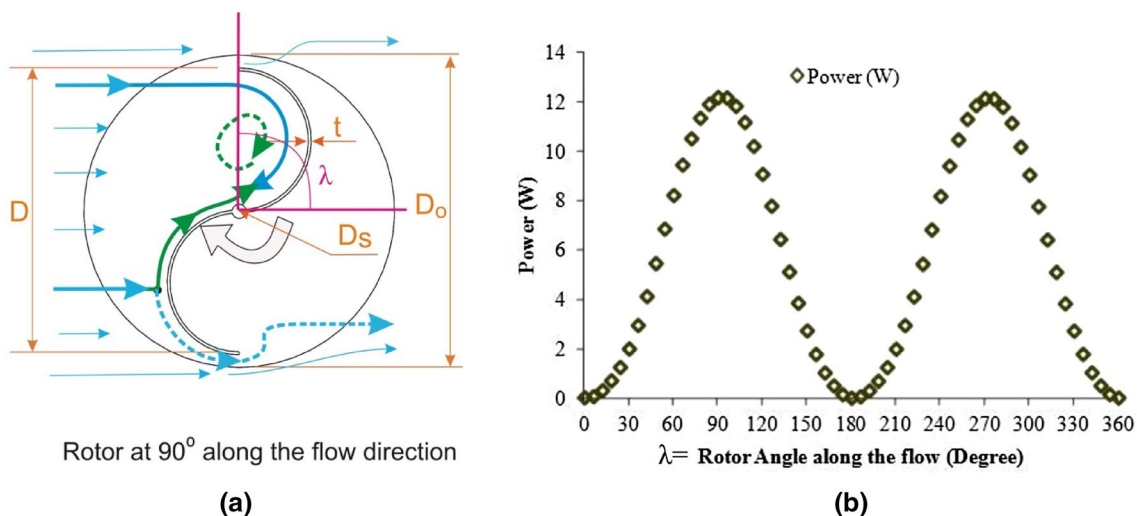


Fig. 2 Power generation at a different angle of the rotor

photographs of manufactured rotors are shown in Fig. 5a. These rotor blades are fabricated from aluminum plates having a 2-mm thickness (t), end plates which cover the axial direction of the rotor are of the same material having a thickness (t_{end}) of 10 mm and a central shaft having a 10-mm diameter (D_s) made up of aluminum. SHKT is designed alike of two semicircular buckets which are placed such that the concave part forms ‘S’ in the shape. The difference in forces subjected due to the fluid medium on convex and concave blades produces drag force; this drag force induces rotation of the hydrokinetic turbine. Despite the low efficiency of SHKT, it is favored as it is simple, compact, easy to install and has low manufacturing cost. The design of SHKT is such that it is independent of flow direction. It rotates omnidirectionally or rotates in a clockwise and anticlockwise direction along the rotor axis. The dimensions used for the rotor diameter (D) are 200 mm; end plate diameter (D_o) is 220 mm and its thickness is 10 mm; the height of the rotor (H) is 180 mm; aspect ratio (AR) is 0.9.

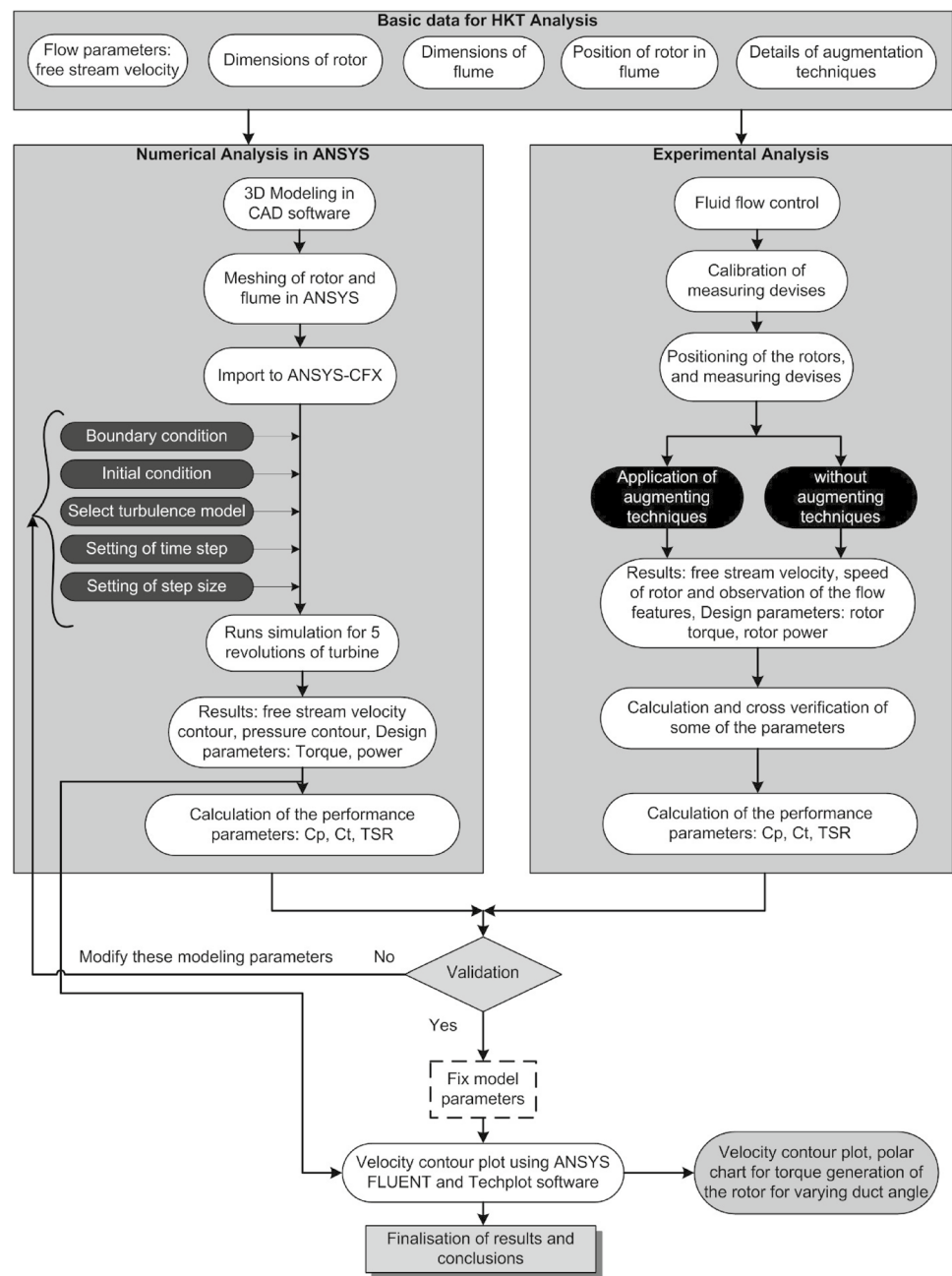
HSHKT has an almost similar specification to the SHKT, the only difference is that the bucket or blade is twisted at any angle along the axis. In this study, HSHKT dimensions remain the same as of SHKT with the same aspect ratio and the angle of twist (θ) is taken as 90° (Fig. 1, Table 4). Through this turbine, the impact of the flow velocity is uninterruptedly exerted positive drag force due to the twisted bucket or blade.

MSHKT has similar design specification as the previous two turbines discussed above. This type of Savonius turbine is basically designed for better performance regarding losses in vortices. The dimensions of rotor diameter, height, angle of twist and aspect ratio remain the same such as 200 mm, 180 mm, 0° and 0.9, respectively. The overlap distance (a) of both the blades is 15 mm apart considering center as the

turbine center axis. The specifications of all the above discussed rotors are shown in Table 4.

Description of the flume is shown in Fig. 5e; also the position of the rotors inside the flume is shown. Inside flume, converging–diverging duct augmentation techniques are used to reduce the fluid flow area of the channels shown in Fig. 5h. In this study, duct angle is kept constant at 29° . However, the duct has the capability to change its angle 20° – 32° . The experiment and numerical analyses are performed considering the distance of the rotor (L) from the initiation of duct convergence as $4D$. For, without duct condition, same distance has been maintained (Fig. 5d). Moreover, in this flume, there are arrangements to set single and double deflector in the flume bed, to provide more flow in the leading edge of the blade of the HKT rotor. The rectangular channel also has provision to provide slope by tilting the flume from 0° to 5° ; however, in this study flume is kept horizontal.

For measuring all the necessary parameters like surface velocity, rotor speed, rotor torque, rotor shaft power, electric power, etc., various devices are installed and connected through the display panel board as shown in Fig. 5g. Panel board consists of all the electrical connections including the output of the sensors. It consists of sensor indicators viz. digital torque indicator, digital speed indicator, and a digital watt indicator. Separately, flow meter and rope brake dynamometer is arranged to measure flow velocity and rotor torque, respectively. The measuring range and uncertainties in measuring devices are provided by the manufacturer. The transducer is attached or circuited to measure torque is strain gauge having a measuring range of the digital torque indicator is 0–6 kg-m having an uncertainty of 1% of full scale. The digital speed indicator works with the help of inductive proximity sensor,

Fig. 3 Flowchart of methodology

measurement of the turbine rotation are in the range of 0.1–3000 rpm associated with the uncertainty of 0.5% of full scale. The digital watt indicator measures electric power generated through the dynamometer and the digital reading is displayed on the panel. The uncertainty which occurs is 0.5% of the full scale.

To measure the free stream velocity (V), the flowmeter is used. The spindle of the flow meter carries cup wheel resting freely on the bearing. The magnetic-type sensor which counts on the one pulse per revolution is attached to the wheel circuited to the microprocessor with alphanumeric LCD. This flowmeter measures in the range of

0–9.999 m/s within the response time of 0–99 s. The calculated uncertainty of the flow meter is 0.1 ± 0.02 m/s.

In the experimental setup, rope brake dynamometer is installed to measure torque (T_{rotor}) as shown in Fig. 5c. Torque corresponding to varying rotor speed can be calculated by this instrument. However, sensors are there to measure the torque and power directly. This measurement device is simple to install and less sensitive to vibrations and alignment of the turbine shaft. The rope brake dynamometer consists of one spring balance which is connected to one end of the rope which passes through the pulley connected with the turbine shaft and another

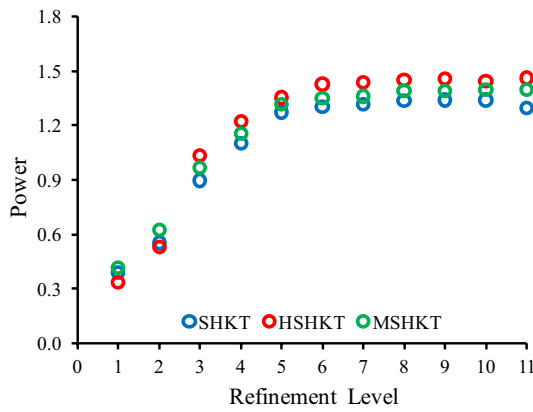


Fig. 4 Variation of power (W) with the different refinement levels

Table 2 Mesh size details of different types of rotor

	Types of rotor		
	SHKT	HSHKT	MSHKT
Mesh details			
Mesh type	Tetrahedral unstructured	Tetrahedral unstructured	Tetrahedral unstructured
In the fluid domain			
Nodes	36,746	41,583	38,896
Elements	189,333	223,468	198,435
In solid domain			
Nodes	867,869	892,725	882,382
Elements	3,161,483	3,320,937	3,141,279

end of the rope is connected to the load. Initially, HKT is rotated at no load conditions. Thereafter, the mechanical loads are applied for different loading conditions. Rotation of the HKT is controlled by the dead weight of the rope brake dynamometer with a certain error in the experiment.

Out of the above, surface stream velocity (V) can be measured and further another design parameter like torque (T) can be calculated. However, the rotor shaft torque can

be measured in this setup directly also along with shaft power (P_{rotor}). Thereafter, other performance parameters will also be calculated with these measured values.

2.3.1 Design parameters

The available torque at the rotor due to the interaction of velocities in upstream and downstream can be expressed as follows.

$$T = 0.5\rho AR(V_1^2 - V_2^2) \tag{1}$$

The available power due to the free stream flow is expressed as follows.

$$P = 0.5\rho AV^3 \times 4a(1 - a)^2, \quad a = (V_1 - V_2)/V_1, \tag{2}$$

where V is the mean free stream velocity, R is the radius of the rotor, ρ is the density of the water ($= 1000 \text{ kg/m}^3$), A is the projected area of the rotor, V_1 and V_2 are the upstream and downstream velocity of the flume.

$$T_{Rotor} = (W_{TS} - W_{SS}) \times g \times (r_p + d_r), \tag{3}$$

The power generated by the rotor is termed as,

$$P_{Rotor} = \frac{2\pi N \times T_{rotor}}{60}, \tag{4}$$

where W_{TS} is the tension in tight side, W_{SS} is the tension in slack side, r_p is the radius of the pulley, d_r is the diameter of the rope, g is the acceleration due to gravity ($= 9.81 \text{ m/s}^2$), ω is the angular velocity of the rotor and N is the number of rotation of the rotor per minute.

The torque generated using rope-brake dynamometer is denoted as rotor torque (T_{Rotor}).

2.3.2 Performance parameters

Tip speed ratio (TSR) is the ratio of the speed of the blade at its tip to the free stream velocity of the water.

Table 3 Detailed options selected for the simulation in ANSYS CFX

S. no.	Options in CFX for stationary	Flume	Options in CFX for rotating	Rotor
1.	Domain type	Fluid domain	Domain motion	Rotating
2.	Flow material	Water	Coordinate frame	Along z axis
3.	Morphology	Continuous fluid	Analysis type	Transient blade row
4.	Domain motion	Stationary	Transient scheme	2 nd Order Backward Euler
5.	Boundary	Interface	Output frequency	Every time-step
6.	Turbulence model	k-Epsilon	Turbulence intensity	Medium (5%)
7.	Wall function	Scalable	Convergence criteria	RMS (1 E^{-4})
8.	Wall roughness	Smooth wall	Advection scheme	Upwind

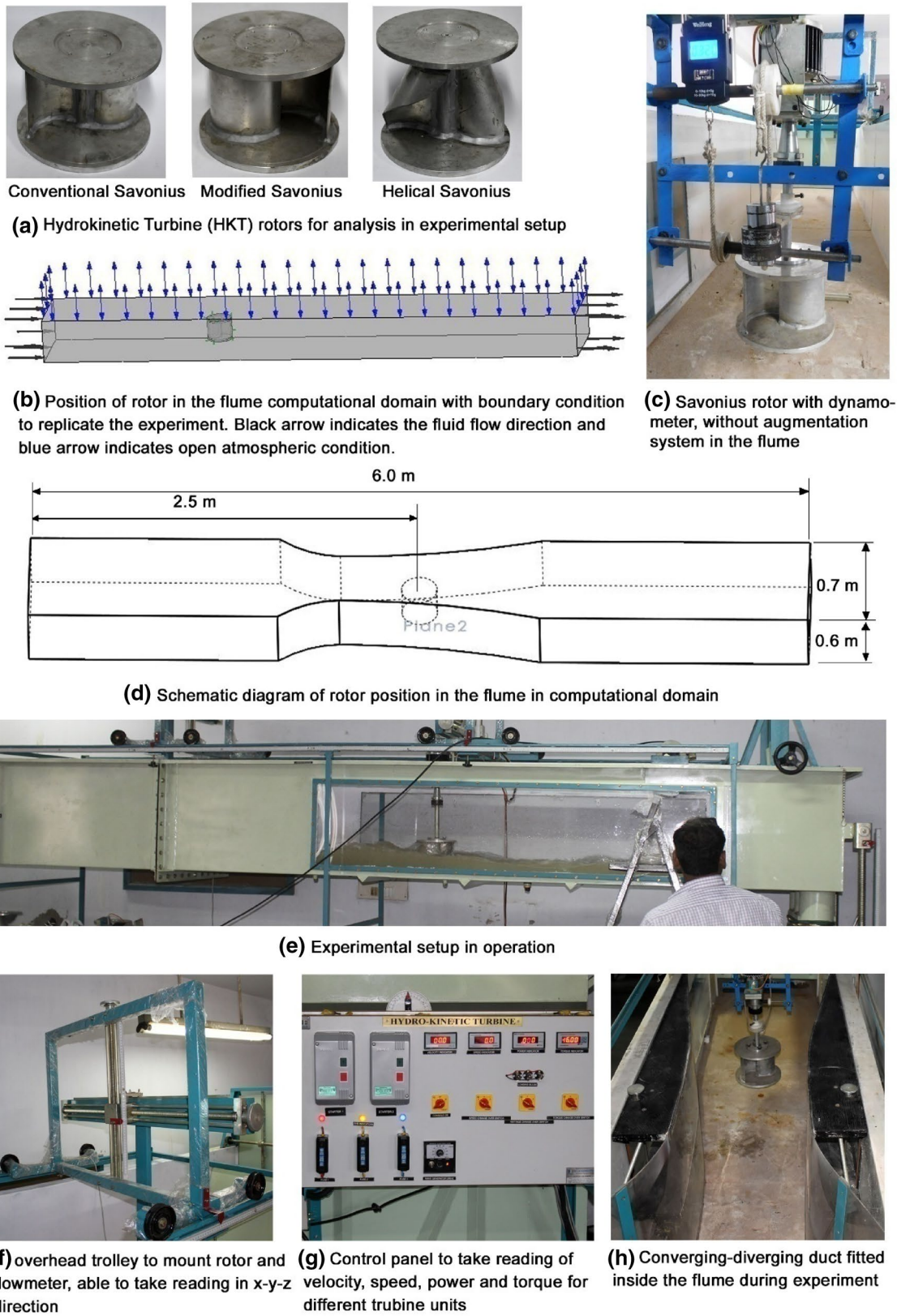


Fig. 5 Experimental setup and its layout for simulation in ANSYS

Table 4 Design specification of Savonius hydrokinetic turbine

Design parameter	Savonius rotor	Modified Savonius rotor	Helical Savonius rotor
Rotor diameter (D)	200 mm	200 mm	200 mm
Rotor height (H)	180 mm	180 mm	196 mm
End plate diameter (D_o)	220 mm	220 mm	220 mm
Shaft diameter (D_s)	10 mm	10 mm	10 mm
Blade thickness (t)	2 mm	2 mm	2 mm
End plate thickness (t_{end})	10 mm	10 mm	10 mm
Overlap distance (a)	0 mm	30 mm	0 mm
Blade shape factor (p/q)	–	–	0.1 (where $p = 12.25$ mm and $q = 122.5$ mm)
Blade arc angle (ψ)	–	–	124°
Twist angle (θ)	0°	0°	90°
Aspect ratio (AR)	0.9	0.9	0.98

$$\text{TSR} = \omega R/V. \quad (5)$$

Coefficient of power (C_p) is the ratio of the power developed by the turbine rotor to the actual power available for the rotor.

$$C_p = \frac{P_{\text{rotor}}}{\rho R H V^3}. \quad (6)$$

Coefficient of torque (C_t) is related to the torque developed by the turbine rotor.

$$C_t = \frac{P_{\text{rotor}}}{\rho R^2 H V^2}. \quad (7)$$

Reynolds number (Re) is the ratio of the inertial force of the fluid medium to the viscous force.

$$\text{Re} = \frac{\rho V R_{C/H}}{\mu}, \quad (8)$$

where

$$R_{C/H} = A_{C/S}/P_{\text{wetted}}, \quad (9)$$

$$\text{Aspect ratio (AR), } \text{AR} = H/D. \quad (10)$$

Froude no. (Fr) is a dimensionless quantity that describes different flow regimes of open channel flow. It is the ratio of inertial forces and gravitational forces. V is the stream velocity and D is the characteristic diameter.

$$\text{Fr} = \frac{V}{\sqrt{g D_{C/H}}}. \quad (11)$$

When $\text{Fr} = 1$, flow is considered as critical; if $\text{Fr} > 1$, flow is Supercritical/shooting/rapid/torrential; if $\text{Fr} < 1$, flow is considered as Subcritical/tranquil/streaming flow.

$$D_{C/H} = \frac{A_{C/S}}{T_{\text{width}}}, \quad (12)$$

Blockage ratio (BR), BR

$$\begin{aligned} &= \frac{\text{Area covered by the rotor}}{\text{Projected flow area in the water channel}} \\ &= \frac{HD}{H_W W}, \end{aligned} \quad (13)$$

where R is the radius of the rotor, H is the height of the rotor, D is the diameter of the rotor, $R_{C/H}$ is the characteristics radius, $A_{C/S}$ is the cross-sectional area of the flow, P_{wetted} is the wetted perimeter of the rotor, U is the free stream velocity (m/s), $D_{C/H}$ is the characteristic diameter (m), T_{width} is the top width of the channel, $A_{C/S}$ is the cross-sectional area of the flow, H_W is the height of the flowing water, W is the width of the channel, ω is the angular velocity of the rotor, R is the radius of the rotor, ρ is the density of the water ($= 1000 \text{ kg/m}^3$).

Turbulence intensity is an important parameter for the computational simulation design. The turbulent intensity of the flow at the specified point can be determined as follows.

$$\text{TI} = \frac{1}{V} \times \sqrt{\frac{1}{3} \{u_x^2 + u_y^2 + u_z^2\}}, \quad (14)$$

where u_x , u_y and u_z are the fluctuation of the velocity in the x -, y - and z -direction, respectively.

Values obtained in the experiment are used to validate some of the results of the numerical study. In addition to this, uncertainty analysis of the results is performed to find out an error range of the data obtained from experiments. Further, the numerical analysis predicts more results, which are beyond the capacity of the experimental setup.

2.3.3 Uncertainty analysis

According to the Moffat uncertainty analysis, the relative error is expressed as based on literature (Moffat 1982, 1988).

Let f is the function which can be expressed as follows.

$$f = X_1^{a_1} \times X_2^{a_2} \times X_3^{a_3} \dots \times X_n^{a_n}. \quad (15)$$

Outcomes having uncertainty is represented as follows.

$$\omega_R = f \times \left[\left\{ \left(\frac{\sum a_1}{x_1} \times \omega_1 \right)^2 + \left(\frac{\sum a_2}{x_2} \times \omega_2 \right)^2 \dots + \left(\frac{\sum a_n}{x_n} \times \omega_n \right)^2 \right\}^{\frac{1}{2}} \right], \quad (16)$$

where $X_1, X_2, X_3 \dots X_n$ are independent sensitive coefficients, $\omega_1, \omega_2, \omega_3 \dots \omega_n$ be the uncertainties in the independent variables, $a_1, a_2, a_3 \dots a_n$ power coefficients of variables.

For the comparative performance of the SHKT, MSHKT and HSHKT rotors in the flume, different independent parameters are measured. Therefore, uncertainty analysis is conducted to find out the relative error on each performance parameter.

3 Result and discussion

In this study, a comparative assessment of the performance of three different types of turbines viz. SHKT, HSHKT and MSHKT is done experimentally and computationally both. These rotors are experimentally tested with and without applying duct in the flume at different turbulent conditions (Re varies from 2.36×10^5 to 3.54×10^5). Whereas, the study is simulated in ANSYS and extended for higher turbulent conditions (Re varies from 2.36×10^5 to 7.08×10^5), which is beyond the experimental capacity. Both experimental and simulation data are compared at a particular case (i.e. $V = 1$ m/s) for validation purpose. Front, top and side views of the simulations of SHKT with the ducted flume for $V = 1$ m/s are shown in Fig. 6a–c. Here, photographs of the rotor are taken as partially submerged condition, to show the flow pattern downstream of the rotor; however, performance results are done for fully submerged conditions (Fig. 5a). It characterizes the velocity profile along the z - x plane. The free stream velocity at the upstream before the ducted area is less than 0.911 m/s. While water passes through the converging duct, it attains a velocity 1.095 m/s. Further, in downstream end velocity reduced to 0.730 m/s. Thus, the free stream velocity enhances available power by striking the advancing blade of the rotor with higher velocity while the duct is installed. Velocity vector at $V = 1$ m/s is shown

in Fig. 6e at 60 rpm and TSR = 0.691. Velocity vector for $V = 2$ m/s and 3 m/s is shown in Fig. 6g and h.

Whereas, experimental output for a similar condition is shown in Fig. 6d and f. Although in this case, rotors are shown in partially submerged condition. However, results for fully submerged rotor conditions are used for comparison. The free stream velocity is 1 ± 0.2 m/s and the rotational speed of the rotor is recorded as 51 rpm. In Fig. 6d, flow passed rotor is shown and it is also found that the hydrodynamic nature of the free stream velocity and surrounding to the SHKT is very much similar to the Fig. 6a. The figure shows a sudden decrement in the water depth at the downstream of the rotor. This indicates total specific energy, i.e., kinetic head and potential head at upstream are converted into the rotational speed of the SHKT. Therefore, the available power of the free stream at the upstream of the rotor is consumed by SHKT and specific energy at downstream reduces. As a result, free stream velocity is also reduced at the downstream of the SHKT.

When the flow of fluid strikes the advancing blade, it experiences a drag force. As a result, positive pressure forms at the upstream of the advancing blade, which helps to rotate the turbine. Simultaneously, at the downstream of the rotor, flow separation occurs at the tip of the advancing blade, towards the direction of flow. As a result, vorticity, i.e., spinning motion of the fluid appears, just downstream of the central part of the rotor and returning blade (Fig. 6f). This creates negative pressure near the downstream of the returning blade. Meanwhile, advancing flow strikes the returning blade also, along the flow direction, with positive pressure. Differences between these pressures are responsible for the rotation of the rotor. As long as negative pressure at the returning blade is more than positive pressure, the turbine rotates. While in the returning blade, the free stream flow impinges on the convex surface which distributes the flow towards the concave surface of the advancing blade and away from the rotor. However, because of the implementation of the duct, the angle of attack of the free stream at the tip of the advancing blade became higher, which helps to overcome the problem to an extent. In Fig. 6i–k, striking of the free stream at a different angle of SHKT blades is captured and free stream pattern surrounding the rotor is captured. When rotor advancing blade is making 0° along the free stream, then wake formation past the rotor is minimum. Whereas, at 90° position of rotor advancing blade creates maximum wake formation, which indicates maximum energy loss in the stream flow.

To evaluate the relative error among measured variables and dependent variables, uncertainty analysis is performed. The uncertainties of the derived variables are calculated based on the theory described in Eqs. (15) and (16). The same for this experimental setup takes the form as

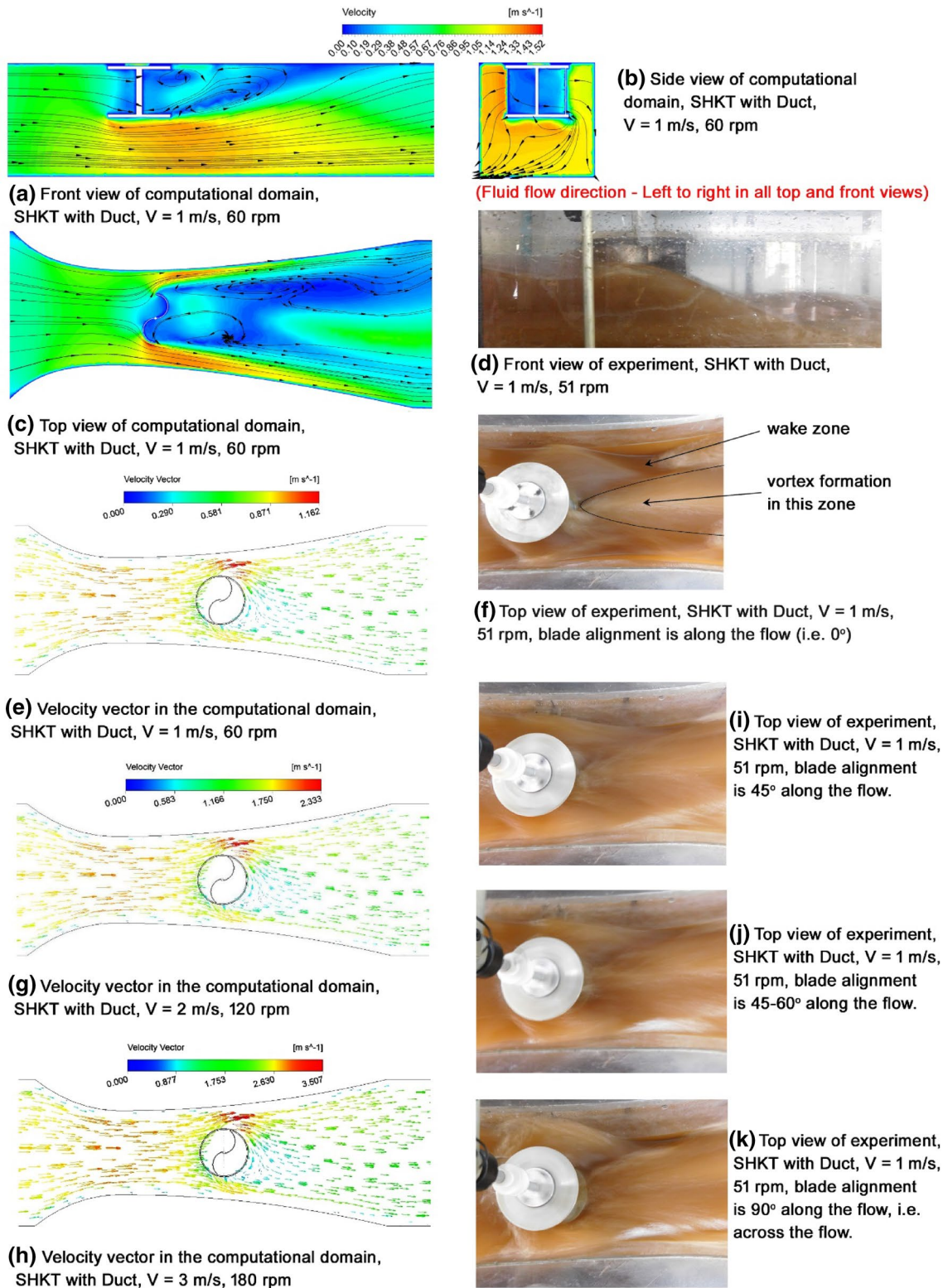


Fig. 6 Different stream flow phenomenon in the computational and experimental domain for SHKT with the duct

Eqs. (17)–(19). The uncertainties in TSR, C_p and C_t of rotor are found 3.05%, 4.39% and 5.35%, respectively.

$$\omega_{TSR} = \sqrt{\left(\frac{R}{V} \times \omega_\omega\right)^2 + \left(\frac{-\omega R}{V^2} \times \omega_\omega\right)^2}, \tag{17}$$

$$\omega_{C_p} = \sqrt{\left(\frac{\omega_{P_{rotor}}}{\rho R H V^3}\right)^2 + \left(\frac{-3V^2 \times \omega_V}{\rho R H V^3}\right)^2}, \tag{18}$$

$$\omega_{C_t} = \sqrt{\left(\frac{\omega_{P_{rotor}}}{\rho R^2 H V^2}\right)^2 + \left(\frac{-2V^{-1} \times \omega_V}{\rho R H V^2}\right)^2}. \tag{19}$$

3.1 Comparison of Savonius HKT, modified Savonius HKT and helical Savonius HKT

A summary of experimental and simulation results obtained for the three different turbines without duct and with duct is shown in Table 5. In Table 4, maximum power (P_{max}) and maximum torque (T_{max}) of different turbines are shown at different free stream velocity. Validation of the numerical analysis is done by the experimental analysis at $V = 1 \pm 0.2$ m/s, for the same initial and boundary conditions.

Numerical simulations show that SHKT generates P_{max} of 1.36 W and T_{max} of 0.21 Nm at 1 m/s free stream velocity without duct condition. Experiments validated the fact with P_{max} of 1.44 W and T_{max} of 0.24 Nm for the same condition. Percentage errors between numerical and

experimental studies of 1 m/s velocity for all the rotors are depicted in Table 4. Percentage calculations are done considering numerical study results as reference/base. Percentage error calculations are done by taking absolute difference of the experimental study and numerical study compared by numerical study (Table 5). Results in Table 1 show the percentage error values of P_{max} and T_{max} are below 6% and 19%, respectively. However, percentage error values of $C_{p_{max}}$ and $C_{t_{max}}$ are below 2.95% and 7.69%, respectively, in reference to Figs. 9, 10 and 11. Thus, numerical studies are considered to be validated with experimental results. In the experimental analysis for the same condition, MSHKT generates 3.47% more P_{max} and 4.17% more T_{max} ; whereas, HSHKT generates 9.72% more P_{max} and 8.33% more T_{max} , respectively. From this discussion, it is found that experimentally HSHKT produces more energy than MSHKT and SHKT. When the duct is implemented, the maximum power and torque production are increased by 24.31% and 29.17% more for MSHKT. In the same condition, the maximum power and torque production are increased by 32.71% and 41.67% more for HSHKT (Table 5). In the numerical study, similar observations are found for predicted values of P_{max} and T_{max} for free stream velocity of 2 m/s and 3 m/s, which are shown in Table 5. It is also observed that without duct condition, for higher free stream velocity, P_{max} and T_{max} of a rotor are obtained at a higher value of rotational speed. When the duct is employed in the channel, P_{max} and T_{max} of the same rotor will be obtained against the further higher value of rotational speed.

Table 5 Maximum power (W) and maximum torque (Nm) of the three different turbines without duct and with duct by varying velocity

Types of the Hydrokinetic turbine	Velocity (m/s)	Without duct		With duct	
		Power (W)	Torque (Nm)	Power (W)	Torque (Nm)
Savonius					
Numerical study	1	1.36	0.21	1.68	0.27
	2	13.62	1.06	15.66	1.21
	3	50.07	2.70	56.64	3.00
Experimental study	1 ± 0.2	1.44	0.24	1.71	0.32
% Error		5.88	14.28	1.78	18.52
Modified Savonius					
Numerical study	1	1.42	0.23	1.97	0.28
	2	13.78	1.10	16.45	1.23
	3	51.49	2.89	60.50	3.10
Experimental study	1 ± 0.2	1.49	0.25	1.95	0.31
% Error		4.92	8.69	1.02	10.7
Helical Savonius					
Numerical study	1	1.51	0.27	2.08	0.33
	2	13.86	1.32	17.45	1.39
	3	59.02	3.30	65.29	3.30
Experimental study	1 ± 0.2	1.58	0.26	2.16	0.34
% Error		4.63	3.70	3.85	3.03

To the study, the insight of the hydrodynamic behavior of the rotor velocity vector (Fig. 7) and pressure plot (Fig. 7) are simulated through ANSYS-CFX. The analyses are done for two different cases, with the implementation of the duct (23° converging angle) and without the implementation of the duct. Velocity ranges with the color band and vector lines for the above-said phenomenon are shown in Fig. 7. Pressure plots are also shown using the color band. In general, uniform pressure is observed throughout the

flume (Fig. 8). When free stream in the upstream interacts with the rotor, stagnation pressure (red in Fig. 8) develops at the upstream of the concave surface of the blade at a low velocity (deep blue in Fig. 7). Simultaneously, at the tip of the advancing blade, flow separation takes place due to the low pressure (green in Fig. 8) (i.e., at high velocity, green in Fig. 7). At the downstream of the rotor, a vortex (here circulation $\Gamma > 0$, therefore, rotation in an anticlockwise direction) is generated at low velocity (blue in Fig. 7),

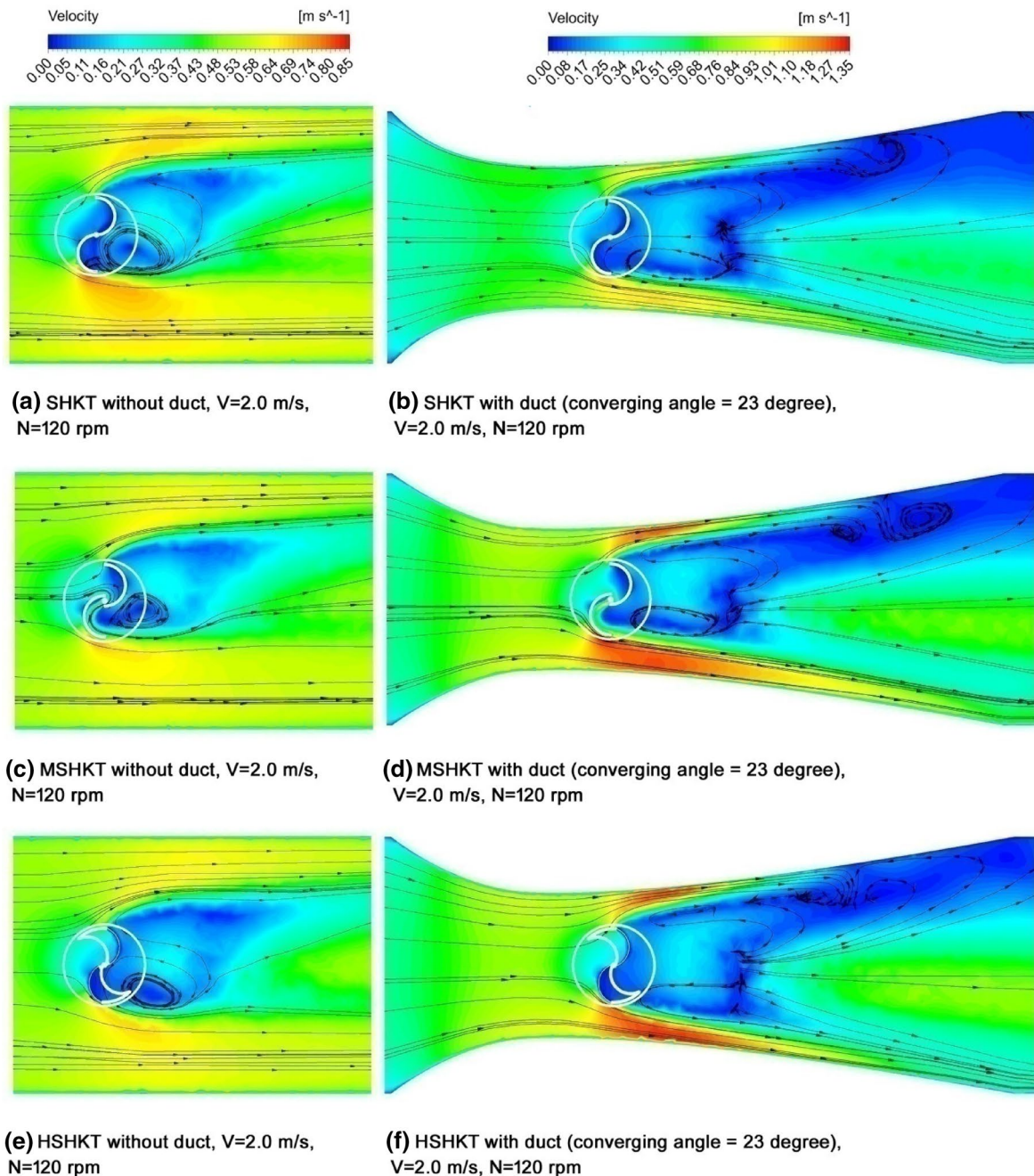


Fig. 7 Velocity color band with a vector contour plot of different rotors with and without duct condition at 2 m/s free stream velocity, $N = 120$ rpm and $TSR = 0.691$

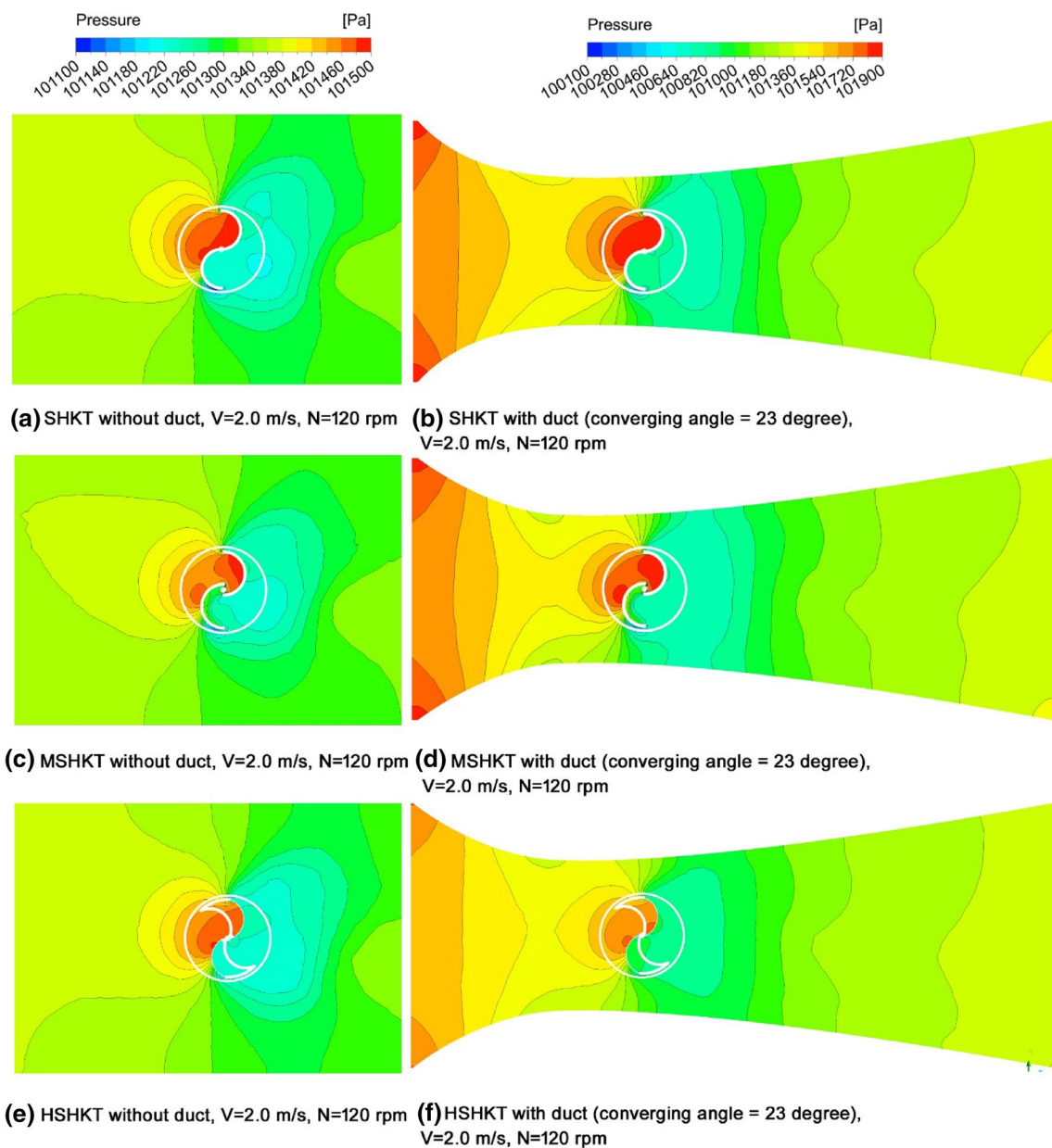


Fig. 8 Pressure developed surrounding the different rotors with and without duct condition at 2 m/s free stream velocity, $N=120$ rpm and $TSR=0.691$

where pressure is also found comparatively low (green in Fig. 8). Moreover, at the upstream of the returning blade, the high-pressure region is found near the convex surface of the returning blade (red and brown in Fig. 8), because of the conflict of rotor rotation direction and free stream velocity movement direction. Whereas, at the downstream of the returning blade, comparatively low-pressure region is obtained (cyan in Fig. 8). Here velocity gets reduced (blue in Fig. 7). Thus, the pressure difference in upstream and downstream regions, near the rotor, also causes rotor rotation (streamline in Fig. 7). Simultaneously, a vortex is formed in

the downstream of the rotor. It is also preferable to extend the formation of the vortex far from the rotor for smooth operation, which is happened in case of HSHKT compared to others (streamlined vortex in Fig. 7e). From the figures, it is observed that, for all three different rotors, at the downstream, low-velocity range (blue in Fig. 7b–f) extends while duct is implemented. Specially, with the implementation of duct, this phenomenon is aggravated in case of HSHKT, where vortex formations almost disappear near the rotor (Fig. 7f). Simultaneously, distance of separation from the rotor towards the downstream direction is also increased,

which is observed from vector contour. It indicates that due to the implementation of the duct, the influence of vortex generated in the downstream has less effect on the torque generation of the rotor. Flow pattern similar to Fig. 7a and c has been reported corresponding to approximately the same free stream velocity for without duct condition (Talukdar et al. 2018; Kumar and Saini 2017). Moreover, from the pressure plot, it is observed that high-pressure zone at the upstream of returning blade is getting reduced in the following order SHKT > MSHKT > HSHKT. It is to be noted that a higher amount of the pressure at upstream of the returning blade creates hindrance in the smooth rotation of the rotor. Therefore, it is obvious that as per design, better performance of the turbine can be obtained in the following order SHKT < MSHKT < HSHKT. Moreover, due to the implementation of the duct, the same is getting reduced for each type of rotors compared to without duct condition. Therefore, it can be declared that the duct helps to improve rotor performance. On the other way, it can be told that as the blockage ratio is increased due to duct implementation,

from 0.086 to 0.150, the performance of the rotors is also increased.

3.1.1 Variation of C_p and C_t with respect to TSR for comparing SHKT with duct and without duct

A performance characteristic of the turbine is explained using the coefficient of power (C_p), coefficient of torque (C_t) and tip speed ratio (TSR). The performance of SHKT with duct and without duct is shown in Fig. 9a–d. A comparative study is conducted between SHKT with duct and SHKT without duct by numerically at the free stream velocity 1 m/s, 2 m/s and 3 m/s. The study is validated experimentally at 1 ± 0.2 m/s free stream velocity. An experimental study is performed initially at no load condition and after each observation mechanical load is increased through rope brake dynamometer. The maximum C_p (i.e. $C_{p_{max}}$) computed numerically at 1 m/s free stream velocity for without duct condition is 0.069 and maximum C_t (i.e. $C_{t_{max}}$) is 0.096 at a TSR value of 0.691. This result is validated through experiment for 1 ± 0.2 m/s free stream velocity. In this case, $C_{p_{max}}$

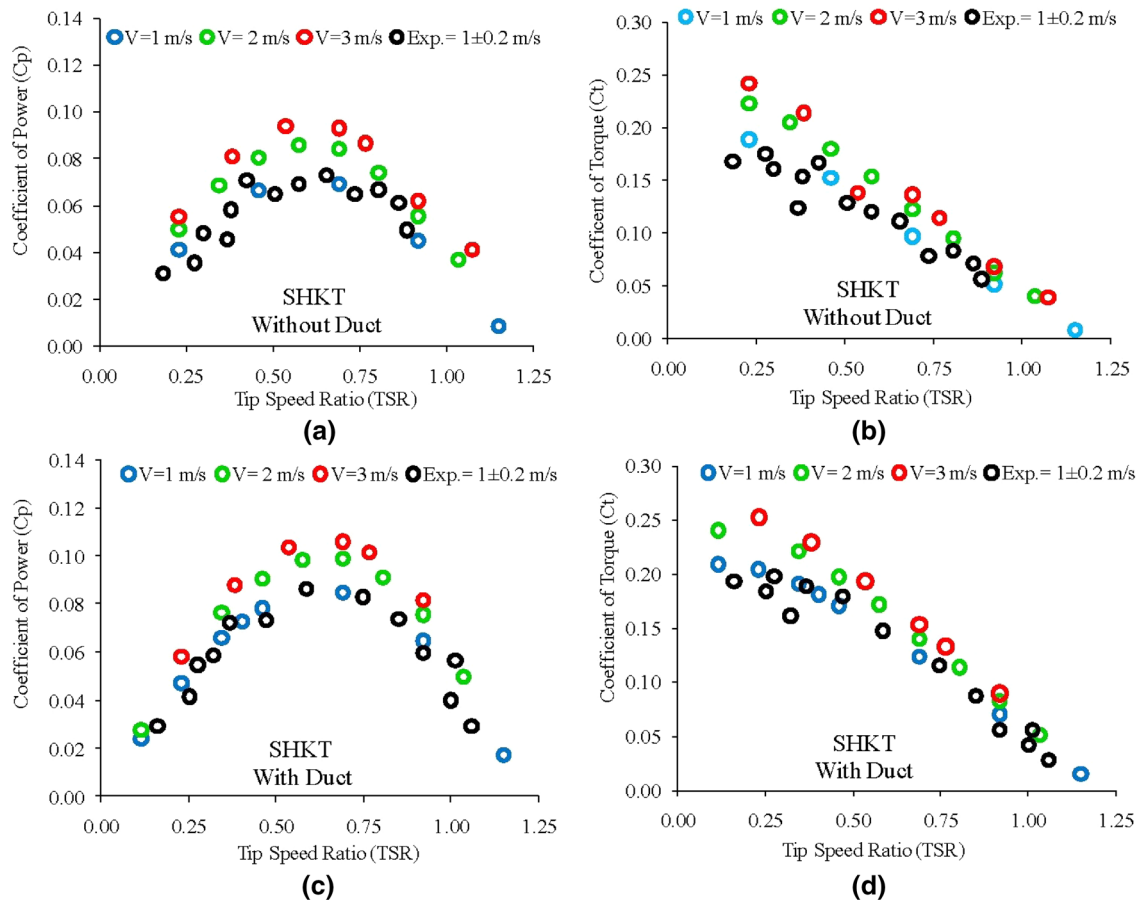


Fig. 9 Effect of different flow velocity on the coefficient of power (C_p), the coefficient of torque (C_t) with respect to tip speed ratio on **a** SHKT without duct, **b** SHKT with duct

and $C_{t_{max}}$ are found 0.073 and 0.111, respectively, at 0.656 TSR. Here, TSR ranges from 0.184 to 0.887. Validation is performed after implementing the duct also, which is shown in Fig. 9c, d. It is found that TSR values are almost independent of the application of the duct. However, overall C_p and C_t increase due to the application of the duct. This suggests that as mainly C_p and C_t increased due to the contraction of inlet area which increases the striking possibility of the flowing water at the advancing blade.

3.2 Variation of C_p and C_t with respect to TSR for comparing MSHKT without duct and with duct

Similar exercise for MSHKT shows that, for 1 ± 0.2 m/s free stream velocity, enhanced $C_{p_{max}}$ and $C_{t_{max}}$ of 2.74% and 3.61% are found for SHKT having without duct condition (Fig. 10a–d). Whereas, if the duct is implemented, the increase of performance is observed as 23.8% $C_{p_{max}}$ and 28.2% $C_{t_{max}}$ more than SHKT without duct condition. Here,

TSR ranges from 0.219 to 1.094. It is observed that at comparatively low TSR, rotors are performing well.

3.3 Variation of C_p and C_t with respect to TSR for comparing HSHKT without duct and with duct

Similar comparison study has been performed for the HSHKT rotor for 1 ± 0.2 m/s free stream velocity. Here, the overall increment in C_p and C_t are observed (Fig. 11a–d). It is found that $C_{p_{max}}$ and $C_{t_{max}}$ are 9.04% and 7.56% more than SHKT without duct condition. For the same rotor, if the duct is implemented, the increment of $C_{p_{max}}$ and $C_{t_{max}}$ is 48.08% and 40.36%, respectively. The experimental result signifies that due to the twisted shape of the rotor blade, it experiences more drag force caused by the flow of fluid for a prolonged period of time. Therefore, C_p and C_t of HSHKT are higher among all the rotors. Performance prediction is also considered numerically for 2 m/s and 3 m/s. For these cases, also increase in C_p and C_t with similar trend curves is found.

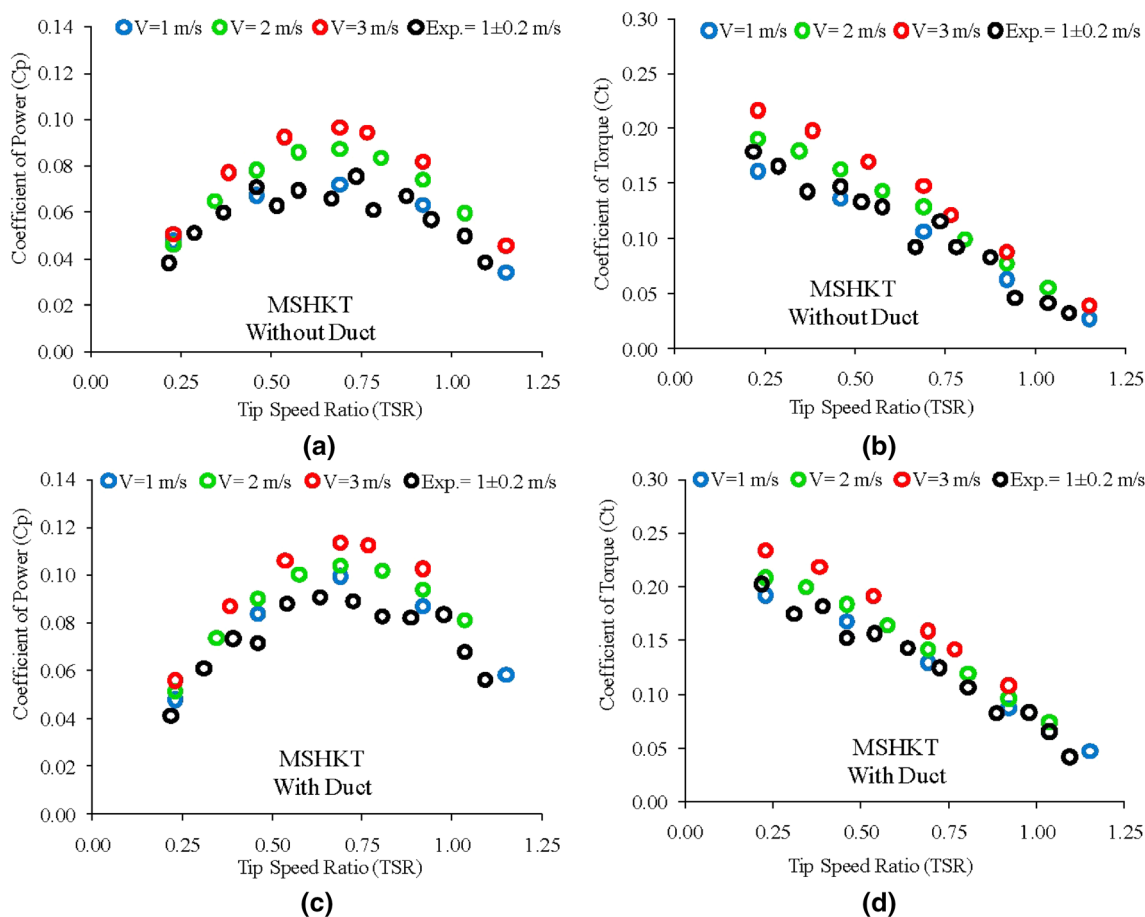


Fig. 10 Effect of different flow velocity on the coefficient of power (C_p), the coefficient of torque (C_t) with respect to tip speed ratio on a MSHKT without duct, b MSHKT with duct

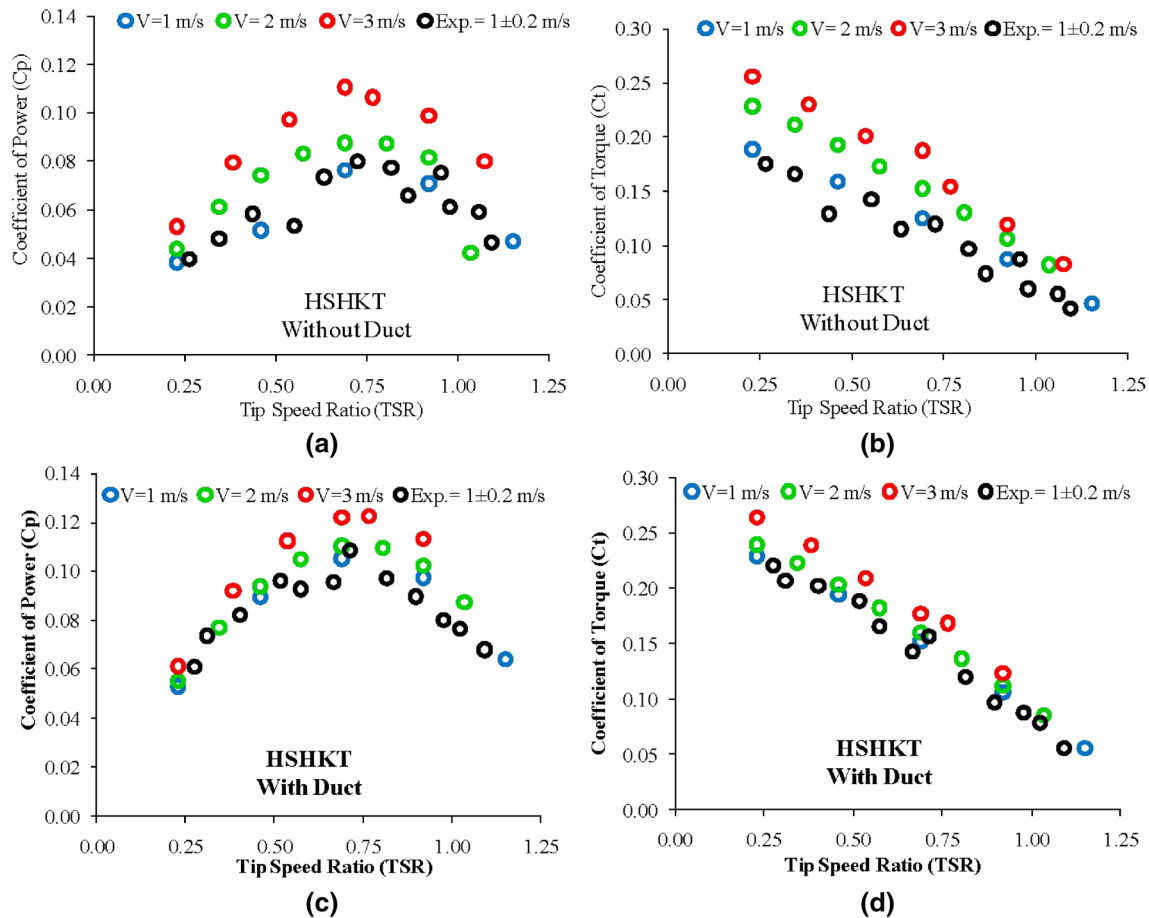


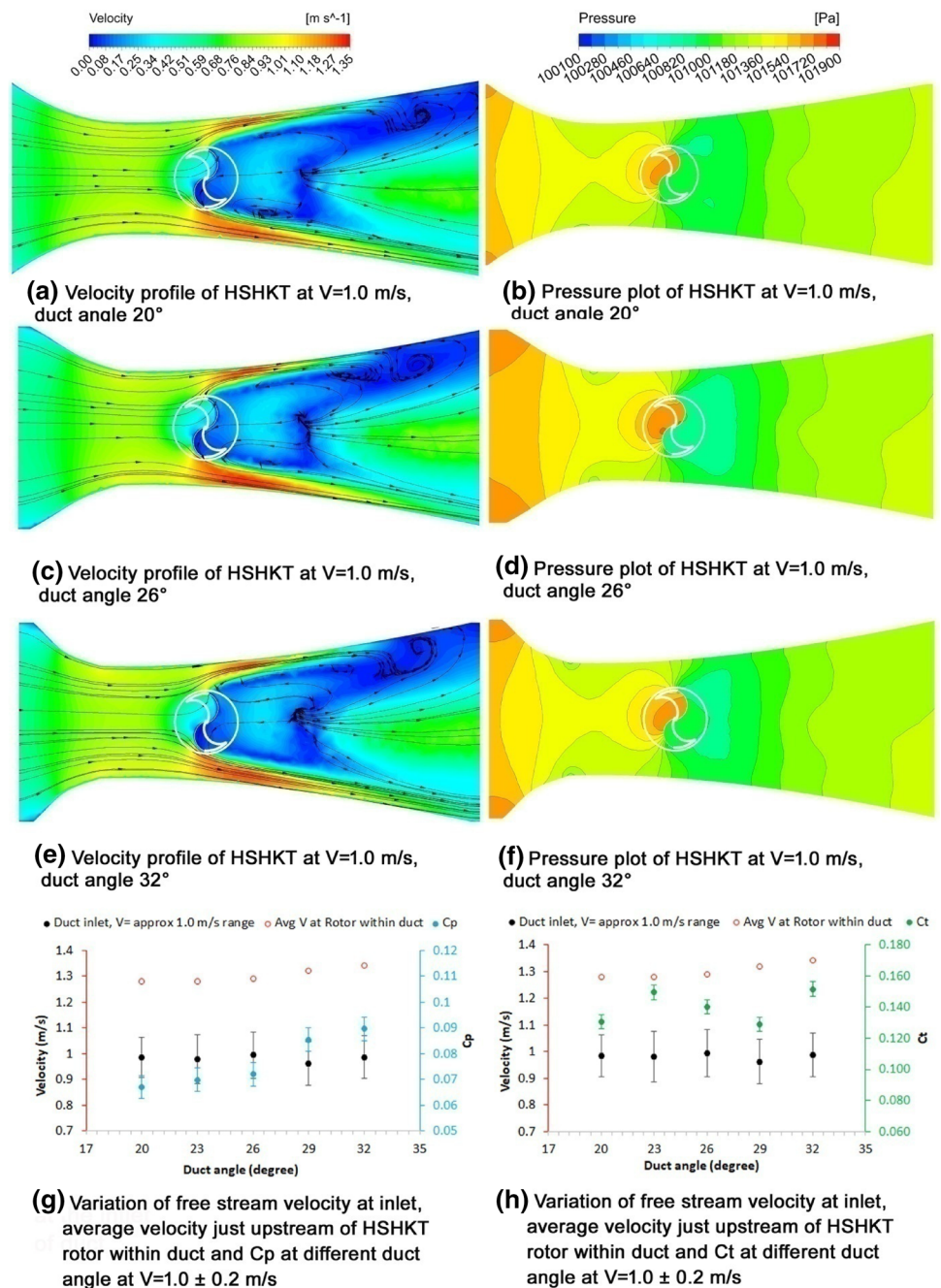
Fig. 11 Effect of different flow velocity on the coefficient of power (C_p), the coefficient of torque (C_t) with respect to tip speed ratio on **a** HSHKT without duct, **b** HSHKT with duct

It is observed from the numerical analysis that for 2 m/s free stream velocity, $C_{p_{max}}$ is increased in the order of 21.74%, 20.83% and 14.47% and $C_{t_{max}}$ is increased in the order of 27.08%, 21.70% and 21.60% for SHKT, MSHKT and HSHKT, respectively. Whereas, for 3 m/s free stream velocity, $C_{p_{max}}$ is increased in the order of 36.23%, 33.33% and 44.74% and $C_{t_{max}}$ is increased in the order of 43.75, 38.68% and 49.60% for SHKT, MSHKT and HSHKT, respectively. From the above discussion, it can be suggested that power generation capacity at the same flow velocity of HSHKT is higher in small amount than SHKT and MSHKT, while considering nearly the same aspect ratio. Instead of higher power generation in Helical Savonius hydrokinetic turbine, the coefficient of power is insignificant changes are observed at the same range of tip speed ratio. Further, a study is conducted to analyze the flow phenomenon around HSHKT with varying duct angle (20° – 32°).

3.4 Flow phenomenon around HSHKT corresponding to varying duct angle

In Fig. 12, analysis of flow behavior around HSHKT with different duct angle varying from 20° to 32° is shown which is validated experimentally also. The experiment and numerical analyses are performed considering the distance of the rotor (L) from the initiation of duct convergence as $4D$. It is observed that while the duct angle increases, the inlet velocity is increased just after the converging section of the duct. For 20° , 23° , 26° , 29° and 32° , an inlet velocity of 1 ± 0.2 m/s increases by 27.5%, 28%, 29%, 32% and 34%, respectively. Significant vortex formation is observed at the downstream of the rotor for lower duct angle (Fig. 12a). When duct angle increases, low-pressure zone formation increases which leads to extend the formation of the vortex far from the rotor (Fig. 12c), and finally disappears (Fig. 12e). Thus, the rotation increases and generates more power. Variation of velocity

Fig. 12 Flow phenomenon around HSHKT and C_p , C_t variation with different duct angle



upstream to the duct, average velocity just downstream of convergences of duct, near the rotor, C_p and C_t are shown in Fig. 12g, h using error graph. In this condition, C_p of HSHKT improves by 28.63%, 16.16%, 43.01%, 50.13% and 82.32% for duct angle of 20° , 23° , 26° , 29° and 32° compared to without duct condition of HSHKT. Thus, to improve the performance of HSHKT, higher duct angle is preferred.

4 Conclusion

In this paper, performances of the Savonius hydrokinetic turbine (SHKT), modified Savonius hydrokinetic turbine (MSHKT) and helical Savonius hydrokinetic turbine (HSHKT) are evaluated and compared for without and with duct condition. Both the numerical and experimental studies are conducted for the performance analysis. The

experimental study validated the performance of the rotor for the free stream velocity of 1 m/s. Whereas, the numerical study extended for 2 m/s and 3 m/s free stream velocity.

- Among all the turbines discussed above, HSHKT generated more power than the other two turbines. The experiment shows that HSHKT without duct generates 1.58 W of P_{\max} and 0.26 Nm of T_{\max} at free stream velocity 1 ± 0.2 m/s. Performance prediction is conducted for the high velocity with the help of numerical analysis. It is observed that for 2 m/s free stream velocity, $C_{p\max}$ is increased in the order of 21.74%, 20.83% and 14.47% and $C_{t\max}$ is increased in the order of 27.08%, 21.70% and 21.60% for SHKT, MSHKT and HSHKT, respectively. Whereas, for 3 m/s free stream velocity, $C_{p\max}$ is increased in the order of 36.23%, 33.33% and 44.74% and $C_{t\max}$ is increased in the order of 43.75%, 38.68% and 49.60% for SHKT, MSHKT and HSHKT, respectively.
- Based on the experimental analysis, HSHKT rotor with duct shows an increment of 48.61% in power and 41.67% in torque as compared with SHKT without duct at same free stream velocity.
- For the HSHKT rotor with duct, the peak value of $C_{p\max}$ and $C_{t\max}$ is 0.108 and 0.156 at TSR 0.714
- Velocity range and vector contour show that, for all three different rotors, at the downstream, low-velocity range extends while duct is implemented. Simultaneously distance of separation from the rotor towards the downstream direction is also increased, which is observed from vector contour. It indicates that due to the implementation of the duct, the influence of vortex generated in the downstream has less effect on the torque generation of the rotor. Thus, when the blockage ratio is increased due to duct implementation, from 0.086 to 0.150, the performances of the rotors are also increased.
- When rotor advancing blade is making 0° along the free stream, then wake formation past the rotor is minimum. Whereas, the 90° position of rotor advancing blade creates maximum wake formation, which indicates maximum energy loss in the stream flow.
- When increasing duct angle, inlet velocity of 1 ± 0.2 m/s increases by 27.5%, 28%, 29%, 32% and 34%, respectively, for duct angle of 20° , 23° , 26° , 29° and 32° . Simultaneously low-pressure zone increases which leads to extend the formation of the vortex far from the rotor. Thus, the performance of the HSHKT is improved at higher duct angle.

In the above section, conclusions of the study are presented. The study shows that HSHKT perform best out of the three Savonius rotors. Duct angle increases turbine performances. Flow phenomenon study shows uniqueness

of power generation from different types of Savonius hydrokinetic rotors and influence of duct augmentation. Simultaneously, role of wake characteristics and vortex formation towards power generation is well explained. Further, study related to rotor design modifications like implementation of adjustable blade, multistaging, influence of aspect ratio, etc. may be considered as the suitable future scopes.

Acknowledgements Authors would like to acknowledge the authority of IIT (ISM), Dhanbad, Jharkhand, India for carryout this study. Authors would like to acknowledge Science and Engineering Research Board (SERB), Govt. of India for funding the Project File No. YSS/2015/001259 to carry out the research work.

References

- Akwa JV, da Silva Junior G A, Petry AP (2012) Discussion on the verification of the overlap ratio influence on performance coefficients of a Savonius wind rotor using computational fluid dynamics. *Renew Energy* 38(1):141–149
- Alidadi M, Calisal S (2014) A numerical method for calculation of power output from ducted vertical axis hydro-current turbines. *Comput Fluids* 105:76–81
- Alom N, Saha UK (2018) Four decades of research into the augmentation techniques of Savonius wind turbine rotor. *J Energy Res Technol* 140(5):050801
- Altan BD, Atilgan M (2008) An experimental and numerical study on the improvement of the performance of Savonius wind rotor. *Energy Convers Manage* 49(12):3425–3432
- Behrouzia F, Maimunb A, Ahmeda YM, Nakisaa M (2015) Novel design of vertical axis current turbine for low current speed via finite volume method. *J Teknol* 74(5):125–128
- Bianchini A, Balduzzi F, Bachant P, Ferrara G, Ferrari L (2017) Effectiveness of two-dimensional CFD simulations for Darrieus VAWTs: a combined numerical and experimental assessment. *Energy Convers Manage* 136:318–328
- Birjandi AH, Bibeau EL, Chatoorgoon V, Kumar A (2013) Power measurement of hydrokinetic turbines with free-surface and blockage effect. *Ocean Eng* 69:9–17
- Cuerva A, Sanz-Andrés A (2005) The extended Betz-Lanchester limit. *Renew Energy* 30(5):783–794
- D'Alessandro V, Montelpare S, Ricci R, Secchiaroli A (2010) Unsteady aerodynamics of a Savonius wind rotor: a new computational approach for the simulation of energy performance. *Energy* 35(8):3349–3363
- do Rio DATD, Vaz JRP, Mesquita ALA, Pinho JT, Junior ACPB (2013) Optimum aerodynamic design for wind turbine blade with a Rankine vortex wake. *Renew energy* 55:296–304
- Driss Z, Mlayeh O, Driss D, Maaloul M, Abid MS (2014) Numerical simulation and experimental validation of the turbulent flow around a small incurved Savonius wind rotor. *Energy* 74:506–517
- Elbatran AH, Ahmed YM, Shehata AS (2017) Performance study of ducted nozzle Savonius water turbine, comparison with conventional Savonius turbine. *Energy* 134:566–584
- Frikha S, Driss Z, Ayadi E, Masmoudi Z, Abid MS (2016) Numerical and experimental characterization of multi-stage Savonius rotors. *Energy* 114:382–404
- Gaden DL, Bibeau EL (2010) A numerical investigation into the effect of diffusers on the performance of hydro kinetic turbines using

- a validated momentum source turbine model. *Renew Energy* 35(6):1152–1158
- Garrett C, Cummins P (2008) Limits to tidal current power. *Renew Energy* 33(11):2485–2490
- Global energy statistical yearbook (2018) <https://yearbook.enerdata.net/electricity/world-electricity-production-statistics.html>. Accessed 23 Dec 2018
- Golecha K, Eldho TI, Prabhu SV (2011) Influence of the deflector plate on the performance of modified Savonius water turbine. *Appl Energy* 88(9):3207–3217
- Golecha K, Eldho TI, Prabhu SV (2012) Performance study of modified Savonius water turbine with two deflector plates. *Int J Rotating Mach* 2012:679247. <https://doi.org/10.1155/2012/679247>
- Gorle JMR, Chatellier L, Pons F, Ba M (2016) Flow and performance analysis of H-Darrieus hydroturbine in a confined flow: a computational and experimental study. *J Fluids Struct* 66:382–402
- Guney MS, Kaygusuz K (2010) Hydrokinetic energy conversion systems: a technology status review. *Renew Sustain Energy Rev* 14(9):2996–3004
- Harries T, Kwan A, Brammer J, Falconer R (2016) Physical testing of performance characteristics of a novel drag-driven vertical axis tidal stream turbine; with comparisons to a conventional Savonius. *Int J Mar Energy* 14:215–228
- Hosseini A, Goudarzi N (2018) CFD analysis of a cross-flow turbine for wind and hydrokinetic applications. In: ASME 2018 international mechanical engineering congress and exposition (pp. V06BT08A044-V06BT08A044). American Society of Mechanical Engineers
- IEA (2018) International energy agency World Energy Outlook 2018. <https://www.iea.org/weo2018/> Accessed 23 Dec 2018
- Kailash G, Eldho TI, Prabhu SV (2012) Study on the interaction between two hydrokinetic Savonius turbines. *Int J Rotating Mach* 2012:581658. <https://doi.org/10.1155/2012/581658>
- Kamoji MA, Kedare SB, Prabhu SV (2009) Experimental investigations on single stage modified Savonius rotor. *Appl Energy* 86(7–8):1064–1073
- Kerikous E, Thevenin D (2019) Optimal shape and position of a thick deflector plate in front of a hydraulic Savonius turbine. *Energy* 189:116157
- Khan MJ, Bhuyan G, Iqbal MT, Quaicoe JE (2009) Hydrokinetic energy conversion systems and assessment of horizontal and vertical axis turbines for river and tidal applications: a technology status review. *Appl Energy* 86(10):1823–1835
- Kumar A, Saini RP (2017) Performance analysis of a Savonius hydrokinetic turbine having twisted blades. *Renew Energy* 108:502–522
- Kumar D, Sarkar S (2016a) A review on the technology, performance, design optimization, reliability, techno-economics and environmental impacts of hydrokinetic energy conversion systems. *Renew Sustain Energy Rev* 58:796–813
- Kumar D, Sarkar S (2016b) Numerical investigation of hydraulic load and stress induced in Savonius hydrokinetic turbine with the effects of augmentation techniques through fluid-structure interaction analysis. *Energy* 116:609–618
- Kumar D, Sarkar S (2017) Modeling of flow-induced stress on helical Savonius hydrokinetic turbine with the effect of augmentation technique at different operating conditions. *Renew Energy* 111:740–748
- Lauder BE, Spalding DB (1983) The numerical computation of turbulent flows. In: Numerical prediction of flow, heat transfer, turbulence and combustion, pp 96–116. Pergamon
- Li LJ, Zhou SJ (2017) Numerical simulation of hydrodynamic performance of blade position-variable hydraulic turbine. *J Hydrodyn* 29(2):314–321
- Maldonado RD, Huerta E, Corona JE, Ceh O, Leon-Castillo AI, Gomez-Acosta MP, Mendoza-Andrade E (2014) Design, simulation and construction of a Savonius wind rotor for subsidized houses in Mexico. *Energy Procedia* 57:691–697
- Malipeddi AR, Chatterjee D (2012) Influence of duct geometry on the performance of Darrieus hydroturbine. *Renew Energy* 43:292–300
- Menet JL (2004) A double-step Savonius rotor for local production of electricity: a design study. *Renew Energy* 29(11):1843–1862
- Moffat RJ (1982) Contributions to the theory of single-sample uncertainty analysis. *J Fluids Eng* 104(2):250–258
- Moffat RJ (1988) Describing the uncertainties in experimental results. *Exp Thermal Fluid Sci* 1(1):3–17
- Mohamed MH, Janiga G, Pap E, Thevenin D (2011) Optimal blade shape of a modified Savonius turbine using an obstacle shielding the returning blade. *Energy Convers Manage* 52(1):236–242
- Nag AK, Sarkar S (2018) Modeling of hybrid energy system for futuristic energy demand of an Indian rural area and their optimal and sensitivity analysis. *Renew Energy* 118:477–488
- Patel V, Eldho TI, Prabhu SV (2019) Velocity and performance correction methodology for hydrokinetic turbines experimented with different geometry of the channel. *Renew Energy* 131:1300–1317
- Ponta F, Dutt GS (2000) An improved vertical-axis water-current turbine incorporating a channelling device. *Renew Energy* 20(2):223–241
- Rauh A, Seelert W (1984) The Betz optimum efficiency for windmills. *Appl Energy* 17(1):15–23
- REN21 (2018) Renewable energy policy network for 21st century. <http://www.ren21.net>. Accessed 23 Dec 2018
- Sarma NK, Biswas A, Misra RD (2014) Experimental and computational evaluation of Savonius hydrokinetic turbine for low velocity condition with comparison to Savonius wind turbine at the same input power. *Energy Convers Manage* 83:88–98
- Shimokawa K, Furukawa A, Okuma K, Matsushita D, Watanabe S (2012) Experimental study on simplification of Darrieus-type hydro turbine with inlet nozzle for extra-low head hydropower utilization. *Renew Energy* 41:376–382
- Talukdar PK, Kulkarni V, Saha UK (2018) Field-testing of model helical-bladed hydrokinetic turbines for small-scale power generation. *Renew Energy* 127:158–167
- The World Bank Data (2018) <https://data.worldbank.org/>. Accessed 23 Dec 2018
- Vennell R (2013) Exceeding the Betz limit with tidal turbines. *Renew Energy* 55:277–285
- Vermaak HJ, Kusakana K, Koko SP (2014) Status of micro-hydrokinetic river technology in rural applications: a review of literature. *Renew Sustain Energy Rev* 29:625–633
- Wahyudi B, Soeparman S, Hoeijmakers HWM (2015) Optimization design of Savonius diffuser blade with moving deflector for hydrokinetic cross flow turbine rotor. *Energy Procedia* 68:244–253
- Yuce MI, Muratoglu A (2015) Hydrokinetic energy conversion systems: a technology status review. *Renew Sustain Energy Rev* 43:72–82